Journal of Alloys and Compounds 1009 (2024) 176971

Contents lists available at ScienceDirect

Journal of Alloys and Compounds

journal homepage: www.elsevier.com/locate/jalcom

Tailoring the coefficient of thermal expansion in a functionally graded material: Al alloyed with Ti-6Al-4V using additive manufacturing

Beril Tonyali [a], Hui Sun [a], Zi-Kui Liu [a], Jayme Keist [a,b], Allison M. Beese [a,c,*]

[a] *Department of Materials Science and Engineering, Pennsylvania State University, University Park, PA 16802, United States*
[b] *Applied Research Laboratory, The Pennsylvania State University, State College, Pennsylvania PA 16803, United States*
[c] *Department of Mechanical Engineering, Pennsylvania State University, University Park, PA 16802, United States*

ARTICLE INFO

Keywords:
Modelling/simulations
Functionally graded materials
Thermal expansion
Aluminum alloys, titanium alloys
Directed energy deposition

ABSTRACT

Functionally graded materials enable the spatial tailoring of properties through controlling compositions and phases that appear as a function of position within a component. The present study investigates the ability to reduce the coefficient of thermal expansion (CTE) of an aluminum alloy, Al 2219, through additions of Ti-6Al-4V. Thermodynamic simulations were used for phase predictions, and homogenization methods were used for CTE predictions of the bulk CTE of samples spanning compositions between 100 wt% Al 2219 and 70 wt% Al 2219 (balance Ti-6Al-4V) in 10 wt% increments. The samples were fabricated using directed energy deposition (DED) additive manufacturing (AM). Al_2Cu and fcc phases were experimentally identified in all samples, and aluminides were shown to form in the samples containing Ti-6Al-4V. Thermomechanical analysis was used to measure the CTE of the samples, which agreed with the predicted CTE values from homogenization methods. The present study demonstrates the ability to tailor the CTEs of samples through compositional modification, thermodynamic calculations, and homogenization methods for property predictions.

1. Introduction

Grading between aluminum alloys and titanium alloys can be beneficial in the aerospace industry for components such as spacecraft shields [1,2], seat-tracks [1,3], beams, bulkheads, fuselage structures, and wing structures [1], all of which must be lightweight, while maintaining high strength and long service lives. However, challenges with the use of these graded materials are their poor machinability [4] and their low toughness at room temperature [5,6] due to the presence of titanium aluminide phases. These challenges can be circumvented by depositing near net shaped components using additive manufacturing (AM) [7].

Recently, researchers have investigated the use of AM to fabricate components that grade between Al alloys sand Ti alloys [8,9]. In laser-based powder-based directed energy deposition (DED) AM, powder metal feedstock is deposited into a melt pool created by a laser heat source, which melts, then rapidly cools and solidifies to the material below. The laser is then moved along a designed tool path in a layer-by-layer fashion until the final part is formed. Key challenges with mixing dissimilar materials in melt-based AM processes include cracking [7,10] due to the formation of intermetallic phases, where transient thermal cycles exacerbate the local stress concentrations and solidification cracking.

Studies exploring the fabrication of functionally graded materials (FGMs) that grade between Al alloys and Ti alloys using DED are limited and have often resulted in cracking. Chen et al. [11] fabricated Ti-6Al-4V / AlSi10Mg bimetallic structures using DED, but intermetallics formed at the interface and resulted in cracking. Hotz et al. [1] fabricated an FGM consisting of layers of AlSi10Mg, then 50% AlSi10Mg with 50% Ti-6Al-4V, followed by layers of Ti-6Al-4V. Cracking at the interfaces between compositions was attributed to formation of intermetallics [1]. Liu et al. [2] graded in 25 vol% compositions steps from 100% Ti-6Al-4V to 100% AlSi10Mg using DED, and cracks were again observed at the composition transitions [2]. Daram et al. [12] studied a graded structure between pure Ti and pure Al fabricated in 10 at% steps using laser powder bed fusion AM and found cracks across the gradient zones due to the presence of intermetallic phases.

In addition to designing compositional pathways that avoid failure during processing due factors such as intermetallic phase formation and hot cracking, efforts are needed in tailoring compositional pathways that result in desired properties. For example, Kirk et al. [13] explored

---

* Corresponding author at: Department of Materials Science and Engineering, Pennsylvania State University, University Park, PA 16802, United States.
E-mail address: beese@matse.psu.edu (A.M. Beese).

https://doi.org/10.1016/j.jallcom.2024.176971
Received 4 August 2024; Received in revised form 6 September 2024; Accepted 10 October 2024

the use of path planning approaches to design an FGM compositional path from Fe95Co5 to Fe10Co60Cr30 with monotonically varying CTE. In their approach, the CTE of a discrete number of compositions within the Fe-Co-Cr ternary space was calculated from a thermodynamic database containing properties, and the CTE of other compositions were linearly interpolated from those data.

Homogenization approaches may also be used to approximate the macroscopic CTE of multiphase alloys based on the phase fractions and individual CTE of those phases that are expected to appear in the material. The simplest approach is the rule of mixtures model [14–16], which is a summation of the volumetric weighted average of the CTE values for each phase and provides the upper bound of bulk CTE. The lower bound for CTE is typically represented with the Turner equation [14,15,17], which takes into consideration the elastic properties of phases in addition to their CTEs and phase fractions. These two homogenization models have been shown to bound the measured CTEs of multiphase materials well in the literature [15].

The goal of the present work is to demonstrate the ability to tailor the CTE as a function of composition and phases in multiphase materials using Al 2219 whose CTE is reduced through additions of Ti-6Al-4V. For this, thermodynamic calculations were used to predict phase fractions as a function of composition, then the CTE of each multiphase composition was predicted using homogenization methods. Monolithic samples of varying ratios of Al 2219 and Ti-6Al-4V were fabricated using DED AM. The compositions, phases, and CTE values were experimentally measured in the monolithic samples. To evaluate the feasibility of fabricating an FGM pillar through the compositions used to tailor CTE between Al 2219 and Ti-6Al-4V, an FGM grading between 100 wt% Al 2219 and 70 wt% Al 2219 / 30 wt% Ti-6Al-4V in 10 wt% Ti-6Al-4V composition increases was fabricated using DED AM, providing insight into the allowable limits of brittle phase in a component to avoid failure in an FGM. The present work demonstrates the ability to use phase and property information to intentionally grade CTE in an FGM; an approach which can be used to design components with desired properties.

2. Materials and methods

2.1. Sample design and fabrication

To probe the design space between Al 2219 and Ti-6Al-4V, thermodynamic predictions of phases, using the open-source MaterialsMap [18] Python library, were performed in the Al-Ti-V ternary, with the results given in the phase heat maps in Fig. 1. Scheil calculations for rapid solidification were used to predict the phases, as these have been shown to accurately capture the phases formed in as-deposited AM components [19,20].

The crack susceptibility criteria [10], which are built into MaterialsMap [18], were calculated across the ternary composition space for the Al-Ti-V system. Three criteria were used to assess crack susceptibility of the compositions of interest: the Kou criterion (Kou), the improved crack susceptibility coefficient (iCSC) criterion, and the simplified Rappaz-Drezet-Gramaud (sRDG) criterion, all of which are described in detail in Ref. [10]. These maps, shown in Fig. 2, were calculated to identify compositions to avoid in designed paths, as they indicate compositions that have relatively high crack susceptibility, which can result in failure during fabrication.

Based on the above design tools, four compositions were selected for fabricating monolithic samples. The designed compositions spanned a region between Al 2219 and Ti-6Al-4V, and were fabricated to evaluate if they resulted in a gradual transition of composition, phases, and a gradual reduction of CTE from that of Al 2219 (see predictions in Fig. 8), with the understanding that gradual variations of CTE would be effective in reducing thermal stresses between gradient layers within an eventual FGM. These compositions also spanned across the ternary space that predicted low crack susceptibility, near the Al-rich corner of the ternary. The four designed compositions were 100 wt% Al 2219, 90 wt% Al 2219 / 10 wt% Ti-6Al-4V, 80 wt% Al 2219 / 20 wt% Ti-6Al-4V, and 70 wt% Al 2219 / 30 wt% Ti-6Al-4V (herein referred to by their Ti-6Al-4V wt%, with the remainder being made up of Al 2219).

The samples were fabricated on a DED AM system (Optomec, LENS MR-7, New Mexico) equipped with ytterbium-doped fiber laser (IPG YLR-500-SM) in an Ar gas environment (< 25 ppm O_2). Gas atomized Al 2219 (Applied Research Laboratory, Pennsylvania) and Ti-6Al-4V

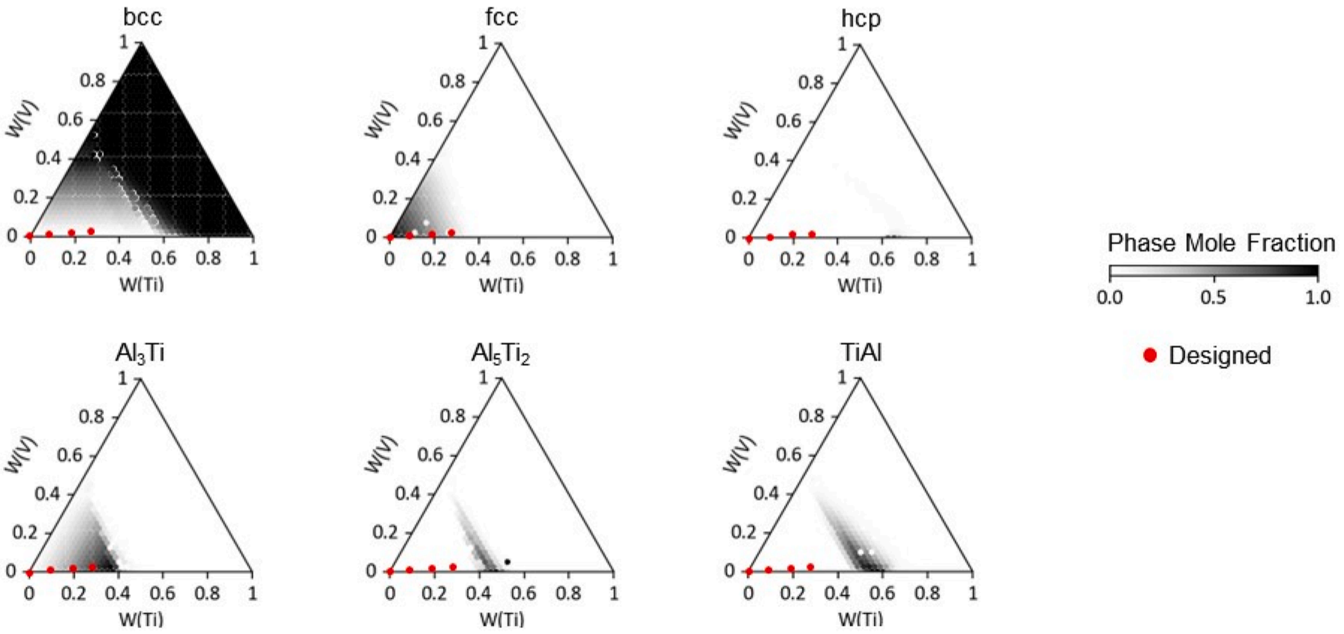

Fig. 1. Phase heatmaps based on Scheil simulations, as a function of composition, in the Al-Ti-V ternary system. The Al-rich corner contains fcc phase and aluminides Al_3Ti, Al_5Ti_2, and TiAl. The Ti- and V- rich corners are made up of solid solution bcc phase. Circle markers on the heatmaps indicate designed compositions of interest fabricated using DED AM.

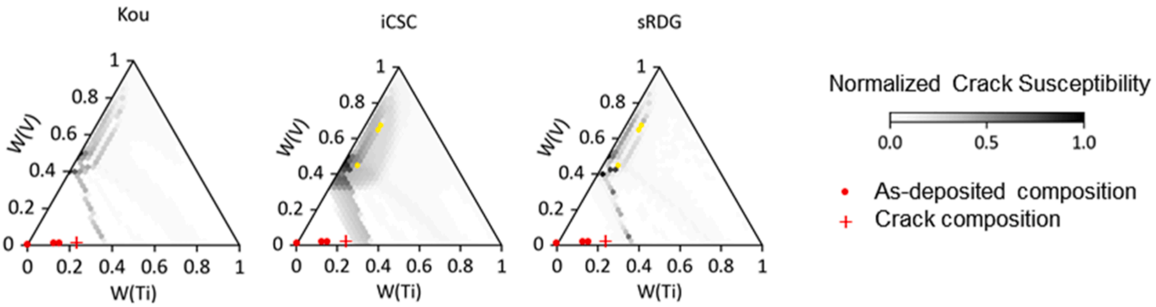

Fig. 2. Normalized crack susceptibility criteria based on the Kou, iCSC, and sRDG criteria for solidification cracking as described in ref. [10], where 0 indicates little crack susceptibility, and 1 indicates the maximum crack susceptibility within the ternary for each of the three considered criteria. Circle symbols correspond to the layer-wise compositions along the FGM sample with the '+' symbol indicating the composition where cracking was experimentally observed.

(Phelly Materials, New Jersey) powders of mesh size −100/+325 were used. The processing parameters, provided in Table 1, were adjusted for each composition to accommodate the addition of Ti-6Al-4V into the respective builds. The fabricated samples were each approximately 8 mm in width, 31 mm in length, and 6–8 mm in height. Brinell hardness tests were performed on the as-deposited samples, with the results confirming that the mechanical properties changed with the addition of Ti-6Al-4V. These hardness data are provided in supplementary Figure S1.

2.2. Experimental methods

The four samples of 0, 10, 20, and 30 wt% Ti-6Al-4V and the FGM pillar fabricated using DED AM were prepared for metallographic evaluation by hot mounting, then polished using standard metallographic preparation techniques, with a 0.05 µm colloidal silica solution final polish. To collect information on the composition of these samples, energy dispersive spectroscopy (EDS, Thermo-Scientific, Apreo S Low Vac, Massachusetts) using a silicon drift detector (Oxford Instruments, Ultim Max silicon drift detector, Massachusetts) was performed. Electron backscatter diffraction (EBSD, Oxford Instruments, Symmetry detector, Massachusetts) paired with image analysis software [21] (MIPAR Image Analysis Software, MIPAR, Ohio) was used to quantify phase information from the samples.

To measure the CTE of the monolithic samples, 10 mm×4 mm round specimens were extracted transverse to the build direction from each of the samples and were tested using a thermal mechanical analyzer (TMA, Q400, TA Instruments, Delaware). These samples were heated per ASTM E228 to 540°C at a heating rate of 5 °C/min, and the length of the samples were measured as a function of temperature throughout the test run at a rate of 1 Hz. To quantify thermal expansion behavior for each sample, the average measured CTE of the samples between 50 and 200 °C were computed and compared with experimentally available data in the literature. Three tests were performed on each sample, and the samples were left to air cool to room temperature between each test run.

Table 1
Processing parameters used in the fabrication of the composition samples with varying Ti-6Al-4V content. Each sample contained 40 layers at a height of 0.02 cm per layer, and each layer contained 15 hatches per layer, at a hatch spacing of 0.05 cm. A laser power of 450 W was used for all samples, with a duty cycle of 100%.

Al 2219 (wt%)	Ti-6Al-4V (wt%)	Travel speed (mm/s)	Powder flow (g/min)
100	0	64	1
90	10	76	1.21
80	20	93	1.39
70	30	105	1.58

2.3. Computational methods

2.3.1. CALPHAD modeling of thermodynamics and input data

An Al-Cu-Ti-V four-element thermodynamic database was constructed for the present study to predict the formation of phases within the composition space spanning from Al 2219 to Ti-6Al-4V. The thermodynamic description contains four binary systems and one ternary system, which were taken from the literature. The binaries included in the database are Al-Cu from Liang et al. [22], Al-Ti from Witusiewicz et al. [23], Al-V from Lindahl et al. [24], and Ti-V from Saunders et al. [25]. The Al-Ti-V ternary system from Lindahl et al. [24] was used. This Al-Ti-V ternary system can provide reliable predictions for Ti-6Al-4V. Additionally, incorporating Cu allows for accurate phase formation representation in Al 2219, which contains 91.5–93.8 wt% Al, 5.8–6.8 wt% Cu, and less than 1 wt% of other elements [26]. Therefore, the major binary and ternary systems included in the present Al-Cu-Ti-V database can capture the phase formation in compositions along an Al 2219 to Ti-6Al-4V gradient in the Al-rich composition.

Using the current Al-Cu-Ti-V database, equilibrium and Scheil simulations were performed to predict phase formation within the DED-fabricated samples. Equilibrium calculations are used to represent one extreme case of solidification, under which a material would undergo infinitely slow cooling. Scheil simulations consider rapid solidification with no diffusion in the solid and perfect mixing of the liquid and have been shown to accurately predict as-deposited phases in additively manufactured components [19,27]. Equilibrium simulations may better capture phase transformations due to in-process thermal cycles and/or post-processing heat treatments of AM components. Together, these two bounds are used to describe phase formation in additively manufactured components. The equilibrium calculations were performed at a temperature of 540°C, which is immediately below the solidus temperature of all compositions under investigation. Scheil solidification simulations start at a temperature at which the material is 100% liquid and end at the eutectic temperature, where the composition is 100% solid, which was calculated to be 548°C for the compositions that were fabricated.

2.3.2. Property predictions

Two different expressions were used to predict the CTE of the compositions as a function of phases across the Al-Ti FGM, i.e., the rule of mixtures equation and the Turner equation for the upper and lower bounds of CTE for the FGM compositions, respectively. The data for phase properties were sourced from the literature and are reported in Table 2. These values were used in the CTE predictions. The rule of mixtures (ROM) approximation is a volumetric dependence of CTE that assumes the behavior of each phase is not influenced by other phases present in a mixture [28] and is represented with the following equation:

$$\overline{\alpha} = \sum \overline{\alpha}_i V_i \tag{1}$$

where $\overline{\alpha}_i$ represent the average CTE across a temperature range of phase

Table 2
Thermo-mechanical property data for the alloys used for fabrication, with phases of which they are composed noted in parentheses, and the aluminide phases that were experimentally found in the samples. The CTE of pure Al 2219 was measured as part of this study and is reported in the table.

Material	CTE, (μm/m · °C)	E (GPa)
Al 2219 (fcc + Al_2Cu)	27.0	70 [31]
Ti−6Al-4V (hcp)	8.8 [32]	114.8 [33]
Al_3Ti	19.5 [34]	209 [35]
TiAl	13 [36]	142 [36]

i, and V_i is the volume fraction of phase i. The Turner [14,15,17] model takes into consideration the interaction between phases through their bonding and stresses produced as a result [17]. With the assumption that the Poisson's ratio is identical between phases, elastic modulus is used in place of bulk modulus in the equation [14], and the Turner equation is given as:

$$\overline{\alpha} = \frac{\sum \overline{\alpha}_i V_i E_i}{\sum V_i E_i} \quad (2)$$

where E_i is the Young's modulus of phase *i*. It is noted that the Turner equation would result in lower CTE predictions over the rule of mixtures due to the consideration of E_i of the phases, in that E_i is lower for phases with higher CTE, and vice versa [14]. Nevertheless, these equations together can be used to bound the property predictions for the monolithic samples, given their phase constituents from thermodynamic predictions and properties of those phases.

2.3.3. Feasibility of Al 2219 / Ti-6Al-4V FGM

To investigate the ability to fabricate an FGM between compositions in which the bulk CTE was designed to change, an FGM from 100 wt% Al 2219 and 70 wt% Al 2219 / 30 wt% Ti-6Al-4V in 10 wt% increments was fabricated using DED with the parameters given in Table 3. As cracking was observed in the samples, crack morphology was analyzed in terms of brittle phase formation and crack susceptibility maps used for path planning. An image of the as-deposited FGM is provided in Fig. 3.

3. Results and discussion

3.1. Experimental characterization

The phases and local compositions were characterized in the samples fabricated with designed ratios of 100 wt% Al 2219, 90 wt% Al 2219 / 10 wt% Ti-6Al-4V, 80 wt% Al 2219 / 20 wt% Ti-6Al-4V and 70 wt% Al 2219 / 30 wt% Ti-6Al-4V. Table 4 gives the nominal designed compositions and as-deposited compositions for each of the samples obtained from EDS, in wt% Ti-6Al-4V. It was determined that the as-deposited compositions were lower in Ti-6Al-4V than designed. The samples with nominal compositions of 10, 20, and 30 wt% Ti-6Al-4V were found to contain 7, 12, and 20 wt% Ti-6Al-4V, respectively. In addition, as shown in the micrographs and EDS maps in Fig. 5, partially unmelted Ti-6Al-4V particles were present in those samples, indicating that not all the deposited Ti-6Al-4V in the sample was completely mixed. These partially unmelted Ti-6Al-4V powder particles were a result of the disparate melting temperature ranges of Ti-6Al-4V (1680-1684°C) and Al 2219 (548-642°C), which led to incomplete melting when the processing for the samples were optimized for Al deposition. These features are also reported in other work grading between pure Al and Ti in the literature [12].

Table 3
Processing parameters used in the fabrication of the FGM sample. Each compositionally distinct region of the sample contained 20 layers at a height of 0.02 cm per layer, and each layer contained 8 hatches per layer, at a hatch spacing of 0.05 cm. A laser power of 437.5 W was used for all samples.

Al 2219 (wt%)	Ti-6Al-4V (wt%)	Travel speed (mm/s)	Duty Cycle (%)	Powder flow (g/min)
100	0	3	50	0.99
90	10	11	100	1.19
80	20	11	100	1.40
70	30	11	100	1.60

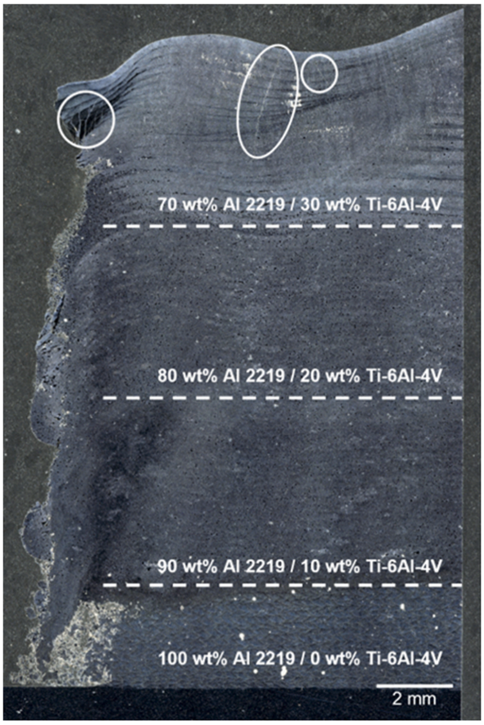

Fig. 3. Optical image of the cross-section of the FGM sample with labels corresponding to the changes in composition along the build direction. Circles indicate locations where cracking was observed in the FGM.

Table 4
Designed sample compositions, their deposited compositions, and compositions of the matrix regions, defined as the regions surrounding the partially melted Ti-6Al-4V particles in fabricated samples. Compositions of the samples are given in wt% Ti-6Al-4V, with the remainder being made up of Al 2219.

Designed Composition, wt% Ti-6Al-4V	Deposited Composition, wt% Ti-6Al-4V	Matrix Composition, wt% Ti-6Al-4V
0	0	0
10	7	3
20	12	3
30	20	6

Localized phase formations were identified in the monolithic samples using EBSD, which are given in Fig. 6. For the monolithic samples containing 7, 12, and 20 wt% Ti-6Al-4V, EBSD results were only obtained from regions surrounding the unmelted particles, as those were the locations where phases would form through solidification and thermal cycling during the DED process. Four different phases were identified in those localized regions: fcc, Al_2Cu, Al_3Ti and TiAl. The 100 wt% Al 2219 sample was made up entirely of Al (fcc) phase and Al_2Cu. X-ray diffraction (XRD) was performed on the FGM sample, which confirmed the phases identified by EBSD as a function of composition (see Figure S2 of the supplemental material).

To quantify the overall phase amounts observed in the samples containing unmelted Ti-6Al-4V particles, which exhibited heterogeneous microstructures, the SEM images shown in Fig. 5(a) for the 7, 12, and 20 wt% Ti-6Al-4V samples were processed using MIPAR image analysis software [21] to distinguish between the four phases that were

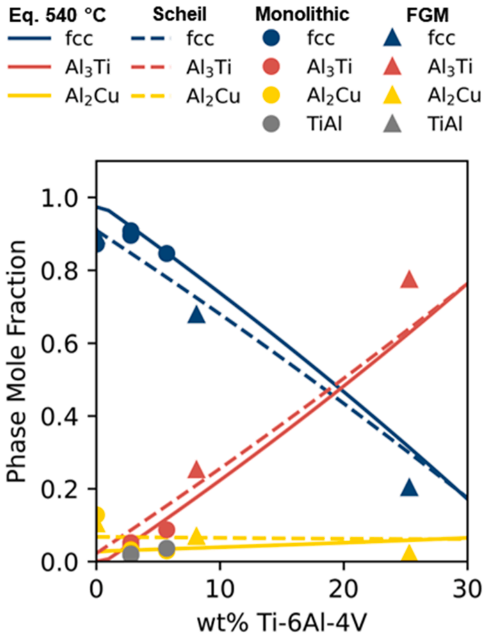

Fig. 4. Experimentally measured phases, in mole fraction, compared with those predicted from equilibrium at 540 °C and Scheil solidification simulations, as a function of wt% Ti-6Al-4V (balance Al 2219). The thermodynamics calculations were made using the Al-Cu-Ti-V database developed in the present work. Data for monolithic samples and the FGM sample are shown by symbols.

observed in EBSD analysis. Due to the inability to distinguish Al (fcc) from Al_2Cu, and TiAl phase from Al_3Ti in the SEM images, local phase fractions for these areas that were identified from EBSD were used to calculate a weighted fraction of fcc and Al_2Cu contained within the areas identified from MIPAR [21] analysis as Al 2219. The same approach was taken to distinguish TiAl from Al_3Ti, which make up the area fraction of aluminides given from the MIPAR [21] analysis. The segmentation of phases from image analysis using this method are shown in Fig. 5(b).

Table 5 presents the calculated phase fractions from EBSD and SEM images that were processed with MIPAR [21]. The 0 wt% Ti-6Al-4V (100 wt% Al 2219) sample consisted of approximately 0.87 mol fraction fcc phase and 0.13 mol fraction Al_2Cu phases, and the other three samples with varying amounts of Ti-6Al-4V (7, 12, 20 wt% Ti-6Al-4V) contained varied amounts of Al_3Ti, TiAl, and Ti-6Al-4V particles in addition to Al (fcc) and Al_2Cu. The amounts of fcc and Al_2Cu phases in these samples decreased with increasing Ti-6Al-4V amount, while Al_3Ti and TiAl phase fractions increased. The amount of unmelted Ti-6Al-4V particles is also reported in the table, which increases with the addition of Ti-6Al-4V in the sample, characteristic of the insufficient melting of Ti-6Al-4V particles during deposition.

As the unmelted Ti-6Al-4V particles would not contribute to the overall phase formation during the DED process, the amount of Ti-6Al-4V that did melt in each of the samples was calculated by subtracting the unmelted Ti-6Al-4V from the overall sample compositions determined by EDS. These compositions, referred to as the matrix compositions, are given in Table 4. As listed in the table, the samples that were intended to contain 10, 20, and 30 wt% Ti-6Al-4V only contained 3, 3, and 6 wt% of melted Ti-6Al-4V that was able to mix during solidification, respectively. To make comparisons between the phases that formed out of the melted matrix phase of the samples, Fig. 4 gives the experimentally observed phase fractions in the matrix phase, i.e. the area surrounding the unmelted Ti-6Al-4V particles, as a function of the matrix compositions that are reported in Table 4. The same trends that were found from the overall sample phase distribution described above are observed in the phases that form in the matrix, where Al (fcc) phase fraction decreases, and Al_3Ti and TiAl phase fractions increase with the addition of Ti-6Al-4V in the melt.

3.2. *Experimental measurements versus CALPHAD predictions*

The amounts of phases present along the designed composition path shown in Fig. 1 are given in Fig. 4 for a composition gradient between 0 and 30 wt% Ti-6Al-4V, balance Al 2219. Equilibrium simulations at 540°C were also used to determine if solid state phase transformations were expected during thermal cycling. As shown, both equilibrium and Scheil simulations predicted fcc, Al_2Cu, and Al_3Ti phase to form. Equilibrium simulations predicted a greater amount of fcc phase to form compared to Scheil simulations over the entire composition range, where Scheil simulations predicted greater fractions of Al_3Ti and Al_2Cu phase than equilibrium calculations.

These thermodynamic predictions were compared to the experimental phase fractions obtained from SEM images, with phases quantified using image processing software [21]. As the layer-wise compositions were assumed to be completely melted and homogenous for Scheil and equilibrium calculations, the presence of unmelted Ti-6Al-4V particles prohibit the direct comparison of predictions with experimentally fabricated samples. Therefore, we compared phases observed in the matrix area of the monolithic samples, i.e., the area surrounding the unmelted particles, with those predicted using thermodynamic calculations.

Fig. 4 compares the experimentally measured phase fractions of the matrix areas of the samples to thermodynamic phase predictions under equilibrium (at 540°C) and Scheil conditions. Equilibrium and Scheil simulations correctly predicted the experimentally observed formation of Al (fcc), Al_2Cu, and Al_3Ti in the monolithic samples, but not TiAl, which is discussed below. The differences in phase fractions predicted by equilibrium and Scheil simulations are small, and all within 8 mol% of experimental values, and therefore within the experimental uncertainty.

The only notable disagreement observed between experiments and predictions was the presence of TiAl phase observed in the experiments, which was not predicted to form in either the equilibrium or Scheil simulations. To characterize these locally observed phases, an EDS line scan was taken from an unmelted Ti-6Al-4V particle to surrounding Al 2219 as shown in Fig. 7(a). This figure highlights the gradients in composition from Ti-6Al-4V to Al 2219 that are observed in areas around the unmelted Ti-6Al-4V particles and the local formation of TiAl and Al_3Ti phases that were observed across these gradients. Therefore, the presence of the TiAl phase is explained by the locally high concentration of Ti around the partially melted particles, where the local composition of Ti exceeded the deposited bulk composition that were used for sample-wise phase predictions shown in Fig. 4.

To confirm the formation of TiAl across the compositions accessed by the line scan from Fig. 7(a), Scheil simulations were performed at compositions from 100% Ti-6Al-4V to 100% Al 2219 and are given in Fig. 7(b). These Scheil simulations predicted the formation of Al_3Ti, TiAl, and Al_5Ti_2 across the composition gradient shown in Fig. 7(a), confirming the expected presence of additional Ti-rich aluminides around the unmelted Ti-6Al-4V particles. EBSD only identifies the presence of Al_3Ti and TiAl due to the similarities in crystal structures between the TiAl and Al_5Ti_2 phases, precluding their differentiation using EBSD. Both phases have tetragonal crystal structures with similar lattice parameters and are at times reported to be the same phase [29]. Local EDS maps of these features show the presence of local compositions that agree with that of Al_5Ti_2. As the TiAl and Al_5Ti_2 phases cannot be distinguished in EBSD, these phases are grouped and reported as TiAl in Fig. 4.

3.3. *TMA measurements and comparison to property predictions*

The experimentally measured CTE of the monolithic samples are compared with the predicted CTE from thermodynamic phase predictions and homogenization methods in Fig. 8. As the Ti-6Al-4V content

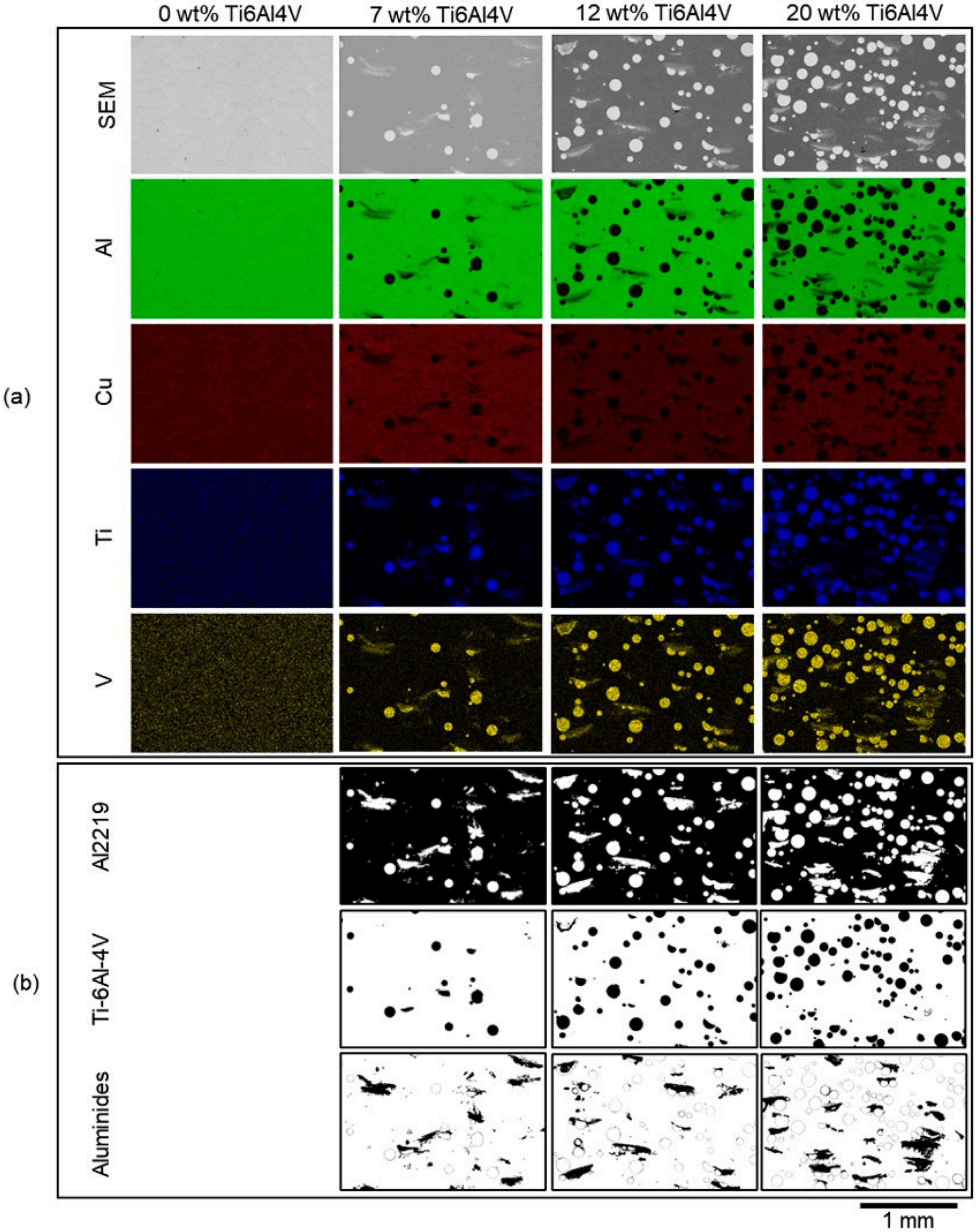

Fig. 5. (a) Backscatter electron images and EDS elemental area maps of monolithic samples with designed compositions varying between 100 wt% Al 2219 and 70 wt% Al 2219 / 30 wt% Ti-6Al-4V in 10 wt% Ti-6Al-4V increments, with actual deposited composition of the overall area noted at the top of the columns. (b) Feature segmentation results using MIPAR image analysis software on the designed 10, 20, and 30 wt% Ti-6Al-4V samples that contained partially melted Ti-6Al-4V particles. The images were segmented to separate features indicative of unmelted Ti-6Al-4V particles, aluminides that surround the particles, which are made up of Al_3Ti and TiAl phases, and the Al 2219 matrix, which is composed of fcc and Al_2Cu.

in the samples increased with respect to Al 2219, the CTE gradually decreased. This decline in CTE was due to increasing amounts of unmelted Ti-6Al-4V particles and the formation of TiAl and Al_3Ti compounds in the samples, all with lower CTEs compared to Al 2219 alloy (see Table 2). The CTE predictions given by the homogenization methods were able to predict the experimental CTE measurements, showing that given accurate phase data, homogenization methods can be used to correctly predict the bounds between which experimental CTE fall.

3.4. FGM path planning and cracking

The as-deposited compositions and phases observed along the FGM pillar grading from 100 wt% Al 2219 to 70 wt% Al 2219 / 30 wt% Ti-

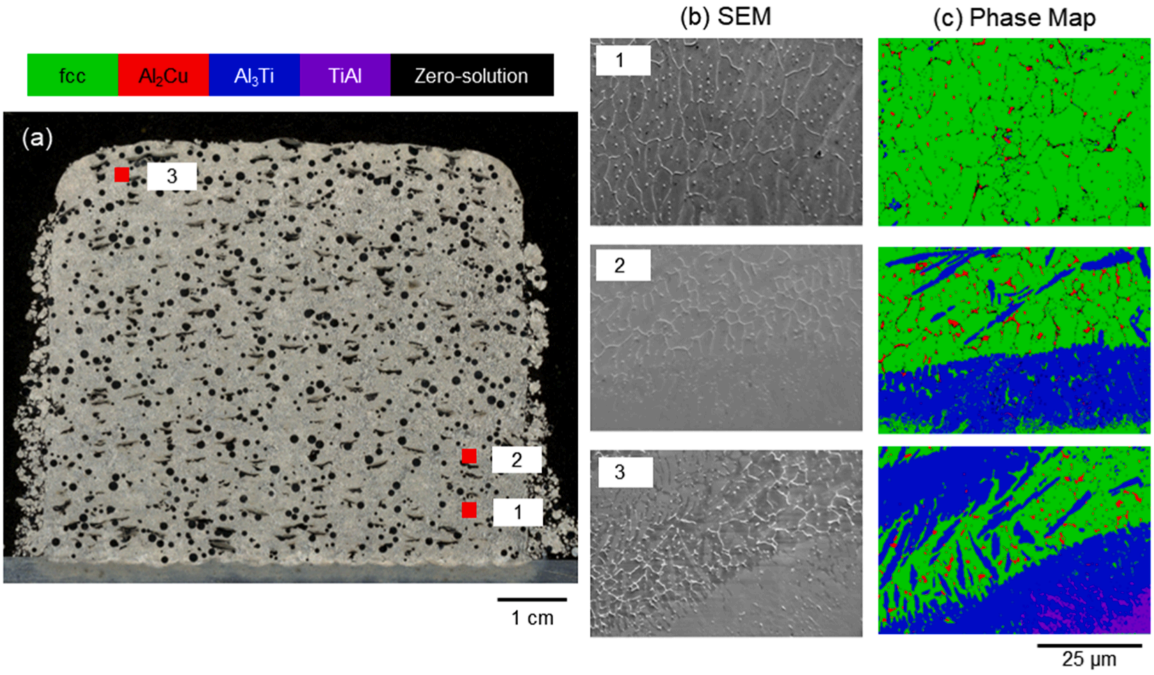

Fig. 6. (a) Optical microscope image of the 80 wt% Al 2219 / 20 wt% Ti-6Al-4V sample where numbers indicate areas analyzed using (b) SEM imaging and (c) EBSD phase analysis. The dark circular features in the optical image of the sample in (a) were confirmed to be unmelted Ti-6Al-4V particles and the elongated dark features were confirmed to be aluminides (i.e., these features are not pores or cracks).

Table 5

Phase mole fractions in monolithic samples containing varying amounts of Ti-6Al-4V calculated with the overall compositions evaluated from SEM backscatter images and EBSD data.

wt% Ti-6Al-4V	Al (fcc)	Al_2Cu	Al_3Ti	TiAl	Ti-6Al-4V
0	0.87	0.13	–	–	–
7	0.88	0.03	0.04	0.02	0.03
12	0.81	0.03	0.05	0.02	0.09
20	0.72	0.03	0.07	0.03	0.15

6Al-4V gradient are given in Table 6. Since the as-fabricated FGM also contained unmelted particles, only the phases in the matrix area were considered for comparison to phase predictions. As shown in Fig. 4, the experimentally observed phases agreed with those given by thermodynamic simulations, providing further validation of the phases present in the Al-Cu-Ti-V system.

The 25 wt% Ti-6Al-4V region of the FGM contained cracking. As the compositions within the FGM did not grade into compositions that were predicted to have high crack susceptibility (see Fig. 2), it is unlikely that the cracking was due to hot cracking during fabrication. It is hypothesized that the cracking was instead a result of the high amount of brittle Al_3Ti phase (77 mol%) relative to the ductile fcc phase present at 25 wt % Ti-6Al-4V. These results confirm that the threshold of brittle phases to

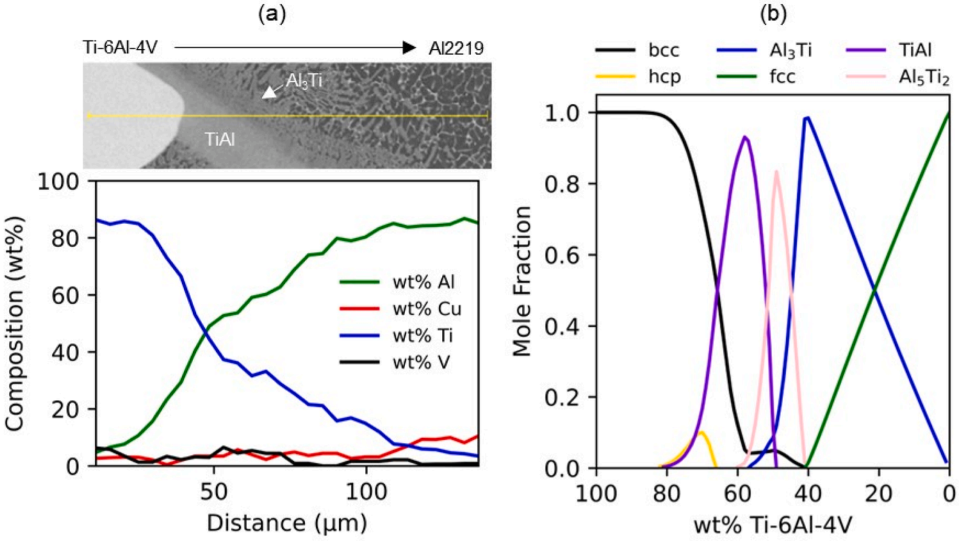

Fig. 7. (a) EDS line scan spanning from an unmelted Ti-6Al-4V particle to an Al 2219 region, which spans from 100% to 0% of Ti-6Al-4V (bal. Al 2219). (b) Scheil phase predictions for pure Al to Ti-6Al-4V, serving as a simplified system to approximate the Ti-6Al-4V to Al 2219 scan.

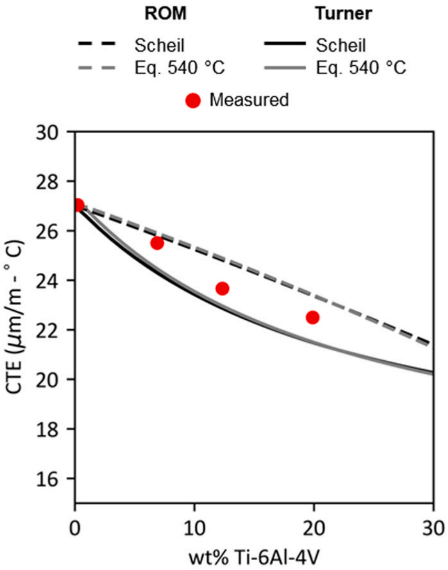

Fig. 8. Experimentally measured CTE as a function of Ti-6Al-4V (balance Al 2219), compared with CTE predictions using the rule of mixtures and Turner equations based on predicted phase fractions from Scheil simulations, equilibrium calculations at 540°C, and experimentally measured phase volume fractions.

Table 6
Phase mole fractions of FGM sample calculated from the compositions evaluated from SEM backscatter images and EBSD data.

wt% Ti-6Al-4V	Al (fcc)	Al_2Cu	Al_3Ti	TiAl	Ti-6Al-4V
0	0.90	0.10	–	–	–
13	0.61	0.04	0.31	0.00	0.05
15	0.57	0.05	0.32	0.01	0.05
25	0.21	0.02	0.77	–	–

avoid cracking is material system-dependent [30], where 32 mol% of Al_3Ti making up the 15 wt% Ti-6Al-4V composition layers in the FGM did not result in cracking but grading to 25 wt% Ti-6Al-4V, resulting in 77 mol%, did.

4. Conclusions

The present work used thermodynamic calculations and homogenization methods to tailor the CTE of Al 2219 through mixing with Ti-6Al-4V. Samples with monolithic compositions spanning between 100 wt% Al 2219 to 80 wt% Al 2219 / 20 wt% Ti-6Al-4V were fabricated using DED AM and were characterized to validate the phase and CTE predictions as a function of the amount of Ti-6Al-4V. An FGM was also fabricated to demonstrate the manufacturability of a functionally graded Al alloy / Ti alloy component. The key findings from the present work are as follows:

- Experimental characterization showed that as the amount of Ti-6Al-4V increased in the monolithic and FGM samples, the amount of fcc phase decreased and the amounts of aluminides increased. These findings agreed with thermodynamic predictions obtained by equilibrium and Scheil simulations.
- Homogenization methods for predicting CTE showed that through incremental additions of Ti-6Al-4V into Al 2219, the CTE of pure Al 2219 alloy is gradually reduced. The CTE measurements for the monolithic samples with varying Ti-6Al-4V content fell in between CTE bounds predicted by homogenization methods, in which the upper bound is given by rule of mixtures predictions and the lower bound is given by the Turner equation. The approach of using phase predictions along with homogenization methods to approximate macroscale properties of compositions can be used in FGM path planning by considering property objectives or constraints in addition to the avoidance of cracking due to phases or solidification in the design of FGM compositional paths.
- Cracking occurred in the FGM sample that graded from 100 wt% Al 2219 to 75 wt% Al 2219 / 25 wt% Ti-6Al-4V due to the high amount of brittle Al_3Ti phase present relative to the ductile matrix phase. This cracking indicates the need to consider critical limits of brittle phases when designing compositions for FGMs to prevent failure.

CRediT authorship contribution statement

Zi-Kui Liu: Writing – review & editing, Resources, Methodology. **Hui Sun:** Writing – review & editing, Software, Investigation, Formal analysis. **Beril Tonyali:** Writing – original draft, Investigation, Formal analysis, Data curation. **Allison M Beese:** Writing – review & editing, Supervision, Resources, Project administration, Methodology, Funding acquisition, Conceptualization. **Jayme Keist:** Writing – review & editing, Resources, Conceptualization.

Declaration of Competing Interest

The authors declare that they have no known competing financial interests or personal relationships that could have appeared to influence the work reported in this paper.

Acknowledgements

B. Tonyali is supported by the Department of Defense (DoD) National Defense Science & Engineering Graduate (NDSEG) Fellowship Program. The authors gratefully acknowledge support from the National Science Foundation (NSF Grant No. CMMI-2050069) and the Office of Naval Research (ONR Grant No. N00014–21–1–2608). The authors thank Mr. Wesley Mitchel at the Applied Research Laboratory – Penn State for helping run experiments.

Appendix A. Supporting information

Supplementary data associated with this article can be found in the online version at doi:10.1016/j.jallcom.2024.176971.

Data Availability

Data will be made available on request.

References

[1] H. Hotz, M. Zimmermann, S. Greco, B. Kirsch, J.C. Aurich, Additive manufacturing of functionally graded Ti-Al structures by laser-based direct energy deposition, J. Manuf. Process 68 (2021) 1524–1534, https://doi.org/10.1016/j.jmapro.2021.06.068.

[2] Y. Liu, C. Liu, W. Liu, Y. Ma, C. Zhang, Q. Cai, B. Liu, Microstructure and properties of Ti/Al lightweight graded material by direct laser deposition, Mater. Sci. Technol. (U. Kingd.) 34 (2018) 945–951, https://doi.org/10.1080/02670836.2017.1412042.

[3] W.V. Vaidya, M. Horstmann, V. Ventzke, B. Petrovski, M. Koçak, R. Kocik, G. Tempus, Improving interfacial properties of a laser beam welded Dissimilar joint of aluminium AA6056 and titanium Ti6Al4V for aeronautical applications, J. Mater. Sci. 45 (2010) 6242–6254, https://doi.org/10.1007/s10853-010-4719-6.

[4] W. Chen, Z. Li, Additive manufacturing of titanium aluminides. Additive Manufacturing for the Aerospace Industry, Elsevier Inc, 2019, pp. 235–263, https://doi.org/10.1016/B978-0-12-814062-8.00013-3.

[5] D. Srivastava, I.T.H. Chang, M.H. Loretto, The effect of process parameters and heat treatment on the microstructure of direct laser fabricated TiAl alloy samples, Intermet. (Barking) 9 (2001) 1003–1013. ⟨www.elsevier.com/locate/intermet⟩.

[6] J. Wang, Z. Pan, D. Cuiuri, H. Li, Phase constituent control and correlated properties of titanium aluminide intermetallic alloys through dual-wire arc additive manufacturing, Mater. Lett. 242 (2019) 111–114, https://doi.org/10.1016/j.matlet.2019.01.112.

[7] D.C. Hofmann, J. Kolodziejska, S. Roberts, R. Otis, R.P. Dillon, J.O. Suh, Z.K. Liu, J. P. Borgonia, Compositionally graded metals: a new frontier of additive manufacturing, J. Mater. Res 29 (2014) 1899–1910, https://doi.org/10.1557/jmr.2014.208.

[8] W. Zhou, C. Shen, X. Hua, Y. Zhang, L. Wang, J. Xin, F. Li, Twin-wire directed energy deposition-arc of Ti–48Al–2Cr–2Nb alloy: feasibility, microstructure, and tensile property investigation, Mater. Sci. Eng.: A 850 (2022), https://doi.org/10.1016/j.msea.2022.143566.

[9] K.O. Abdulrahman, E.T. Akinlabi, R.M. Mahamood, S. Pityana, M. Tlotleng, Laser Metal Deposition Of Titanium Aluminide Composites: A Review, Mater Today Proc 5 (2018) 19738–19746, https://doi.org/10.1016/j.matpr.2018.06.336.

[10] Z. Yang, H. Sun, Z.-K. Liu, A.M. Beese, Design methodology for functionally graded materials: Framework for considering cracking, Addit. Manuf. 73 (2023) 103672, https://doi.org/10.1016/j.addma.2023.103672.

[11] B. Chen, T. Wang, X. Xi, C. Tan, X. Song, Additive manufacturing of Ti-Al functionally graded material by laser based directed energy deposition, Rapid Prototyp. J. 29 (2022) 558–568, https://doi.org/10.1108/RPJ-04-2022-0117.

[12] P. Daram, A. Singh, T. Hiroto, T. Kitashima, M. Watanabe, Compositionally graded titanium to aluminum processed by laser powder bed fusion process: microstructure evolution and mechanical properties, Mater. Sci. Eng.: A 903 (2024), https://doi.org/10.1016/j.msea.2024.146638.

[13] T. Kirk, R. Malak, R. Arroyave, Computational design of compositionally graded alloys for property monotonicity, J. Mech. Des., Trans. ASME 143 (2021), https://doi.org/10.1115/1.4048627.

[14] M.S.A. Karunaratne, S. Kyaw, A. Jones, R. Morrell, R.C. Thomson, Modelling the coefficient of thermal expansion in Ni-based superalloys and bond coatings, J. Mater. Sci. 51 (2016) 4213–4226, https://doi.org/10.1007/s10853-015-9554-3.

[15] C.L. Hsieh, W.H. Tuan, Thermal expansion behavior of a model ceramic-metal composite, Mater. Sci. Eng. A 460–461 (2007) 453–458, https://doi.org/10.1016/j.msea.2007.01.109.

[16] S.H. Ryu, J.H. Park, C.S. Lee, J.C. Lee, S.H. Ahn, S.T. Oh, Experimental measurement of coefficient of thermal expansion for graded layers in Ni-Al2O3 FGM joints for accurate residual stress analysis, Mater. Trans. 50 (2009) 1553–1557, https://doi.org/10.2320/matertrans.M2009028.

[17] P.S. Turner, Thermal-Expansion Stresses in Reinforced Plastics 1, 1745.

[18] H. Sun, B. Pan, Z. Yang, A.M. Krajewski, B. Bocklund, S.-L. Shang, J. Li, A.M. Beese, Z.-K. Liu, MaterialsMap: A CALPHAD-based tool to design composition pathways through feasibility map for desired dissimilar materials, demonstrated with resistance spot welding joining of Ag-Al-Cu, Mater. (Oxf.) 36 (2024) 102153, https://doi.org/10.1016/j.mtla.2024.102153.

[19] B. Bocklund, L.D. Bobbio, R.A. Otis, A.M. Beese, Z.K. Liu, Experimental validation of Scheil–Gulliver simulations for gradient path planning in additively manufactured functionally graded materials, Mater. (Oxf.) 11 (2020), https://doi.org/10.1016/j.mtla.2020.100689.

[20] B. Tonyali, H. Sun, B. Bocklund, J.P. Borgonia, R.A. Otis, S.L. Shang, Z.K. Liu, A. M. Beese, Additively manufactured Ni-20Cr to V functionally graded material: Computational predictions and experimental verification of phase formations, J Alloys Compd 985 (2024), https://doi.org/10.1016/j.jallcom.2024.174011.

[21] J.M. Sosa, D.E. Huber, B. Welk, H.L. Fraser, Development and application of MIPAR™: a novel software package for two- and three-dimensional microstructural characterization, Integr. Mater. Manuf. Innov. 3 (2014) 123–140, https://doi.org/10.1186/2193-9772-3-10.

[22] S.-M. Liang, R. Schmid-Fetzer, Thermodynamic assessment of the Al–Cu–Zn system, part II: Al–Cu binary system, Calphad 51 (2015) 252–260, https://doi.org/10.1016/j.calphad.2015.10.004.

[23] V.T. Witusiewicz, A.A. Bondar, U. Hecht, S. Rex, T.Ya Velikanova, The Al–B–Nb–Ti system: III. Thermodynamic re-evaluation of the constituent binary system Al–Ti, J. Alloy. Compd. 465 (2008) 64–77, https://doi.org/10.1016/j.jallcom.2007.10.061.

[24] B. Lindahl, X.L. Liu, Z.-K. Liu, M. Selleby, A thermodynamic re-assessment of Al–V toward an assessment of the ternary Al–Ti–V system, Calphad 51 (2015) 75–88, https://doi.org/10.1016/j.calphad.2015.07.002.

[25] I. Ansara, A.T. Dinsdale, M.H. Rand, Thermochemical database for light metals alloys, Office for Official Publications of the European Communities, Luxembourg, 1998.

[26] Aluminum standard and data, (2000).

[27] B. Tonyali, H. Sun, B. Bocklund, J.P. Borgonia, R.A. Otis, S.L. Shang, Z.K. Liu, A. M. Beese, Additively manufactured Ni-20Cr to V functionally graded material: computational predictions and experimental verification of phase formations, J. Alloy. Compd. 985 (2024), https://doi.org/10.1016/j.jallcom.2024.174011.

[28] H.A. Bruck, B.H. Rabin, Evaluation of rule-of-mixtures predictions of thermal expansion in powder-processed Ni-Al2O3 composites, J. Am. Ceram. Soc. 82 (1999) 2927–2930, https://doi.org/10.1111/j.1151-2916.1999.tb02182.x.

[29] J.C. Schuster, M. Palm, Reassessment of the binary aluminum-titanium phase diagram, J. Phase Equilibria Diffus 27 (2006) 255–277, https://doi.org/10.1361/154770306X109809.

[30] L.D. Bobbio, R.A. Otis, J.P. Borgonia, R.P. Dillon, A.A. Shapiro, Z.K. Liu, A. M. Beese, Additive manufacturing of a functionally graded material from Ti-6Al-4V to Invar: Experimental characterization and thermodynamic calculations, Acta Mater. 127 (2017) 133–142, https://doi.org/10.1016/j.actamat.2016.12.070.

[31] Properties and Selection: Nonferrous Alloys and Special-Purpose Materials, ASM International, 1990. https://doi.org/10.31399/asm.hb.v02.9781627081627.

[32] P. Rangaswamy, M.B. Prime, M. Daymond, M.A.M. Bourke, B. Clausen, H. Choo, N. Jayaraman, Comparison of residual strains measured by X-ray and neutron diffraction in a titanium (Ti-6Al-4V) matrix composite, Mater. Sci. Eng. A 259 (1999) 209–219, https://doi.org/10.1016/S0921-5093(98)00893-4.

[33] J.S. Keist, T.A. Palmer, Role of geometry on properties of additively manufactured Ti-6Al-4V structures fabricated using laser based directed energy deposition, Mater. Des. 106 (2016) 482–494, https://doi.org/10.1016/j.matdes.2016.05.045.

[34] J. Qin, G. Chen, X. Ji, X. Song, N. Hu, F. Han, Z. Du, Effect of reaction temperature on the microstructures and mechanical properties of high-intensity ultrasonic assisted in-situ Al3Ti/2024 Al composites, J. Alloy. Compd. 666 (2016) 58–64, https://doi.org/10.1016/j.jallcom.2016.01.121.

[35] Y. Cao, N. Wei, X. Han, C. Guo, J. Du, W. He, J. Ma, F. Jiang, Mechanical response of titanium tri-aluminide intermetallic alloy, Mater. Sci. Eng. A 706 (2017) 242–248, https://doi.org/10.1016/j.msea.2017.09.015.

[36] W. Sun, F. You, F. Kong, X. Wang, Y. Chen, Effect of residual stresses on the mechanical properties of Ti-TiAl laminate composites fabricated by hot-pack rolling, Mater. Charact. 166 (2020), https://doi.org/10.1016/j.matchar.2020.110394.